

RESEARCH ARTICLE

SPECIAL ISSUE: RECONSTITUTING CELL BIOLOGY

Myosin-II activity generates a dynamic steady state with continuous actin turnover in a minimal actin cortex

Sonal, Kristina A. Ganzinger*, Sven K. Vogel, Jonas Mücksch, Philipp Blumhardt and Petra Schwille†

ABSTRACT

Dynamic reorganization of the actomyosin cytoskeleton allows fast modulation of the cell surface, which is vital for many cellular functions. Myosin-II motors generate the forces required for this remodeling by imparting contractility to actin networks. However, myosin-II activity might also have a more indirect contribution to cytoskeletal dynamics; it has been proposed that myosin activity increases actin turnover in various cellular contexts, presumably by enhancing disassembly. *In vitro* reconstitution of actomyosin networks has confirmed the role of myosin in actin network disassembly, but the reassembly of actin in these assays was limited by factors such as diffusional constraints and the use of stabilized actin filaments. Here, we present the reconstitution of a minimal dynamic actin cortex, where actin polymerization is catalyzed on the membrane in the presence of myosin-II activity. We demonstrate that myosin activity leads to disassembly and redistribution in this simplified cortex. Consequently, a new dynamic steady state emerges in which the actin network undergoes constant turnover. Our findings suggest a multifaceted role of myosin-II in the dynamics of the eukaryotic actin cortex.

This article has an associated First Person interview with the first author of the paper.

KEY WORDS: WASP, Cytoskeletal dynamics, *In vitro* reconstitution, Supported lipid bilayer, Synthetic biology

INTRODUCTION

Rapid and controlled modulation of cell shape provides the foundation for cellular functions such as division, growth, migration and adhesion. In eukaryotic cells, much of this modulation can be attributed to the dynamics of the actomyosin cortex that lines the inner surface of the plasma membrane. The cortex is a thin network of actin filaments associated with myosin motors (see Salbreux et al., 2012 for a comprehensive review). It is further reinforced by a collection of actin-binding proteins that mediate filament–filament and filament–membrane interactions. Additionally, myosin-II motors drive contractility of the actin meshwork, generating forces at different length scales that enable fast remodeling of the cell surface.

Max Planck Institute of Biochemistry, 82152 Martinsried, Germany.

*Present address: Physics of Cellular Interactions Group, Living Matter Department, AMOLF, 1009 DB Amsterdam, The Netherlands.

†Author for correspondence (schwille@biochem.mpg.de)

ORCID iD: S., 0000-0002-2361-4131; K.A.G., 0000-0001-9106-9406; S.K.V., 0000-0003-2540-5947; J.M., 0000-0002-1469-6956; P.B., 0000-0001-5510-4809; P.S., 0000-0002-6106-4847

This is an Open Access article distributed under the terms of the Creative Commons Attribution License (<https://creativecommons.org/licenses/by/4.0>), which permits unrestricted use, distribution and reproduction in any medium provided that the original work is properly attributed.

Received 2 May 2018; Accepted 16 October 2018

Another factor that imparts dynamicity to the cortex is the continuous turnover of all the protein components of this network. Relative rates of turnover can determine the mechanical properties of the cortex and are, therefore, subject to local regulation. For instance, actin turnover has a significant effect on cortical tension (Tinevez et al., 2009), and various network elements are implicated in imparting different turnover rates to subpopulations of actin (Fritzsche et al., 2013). The rate of actin turnover even within the same cell varies between functionally distinct regions of the cortex (Murthy and Wadsworth, 2005). Actin turnover rates can be tuned by manipulation of either assembly or disassembly processes. Lipids in the membrane can orchestrate local polymerization via activation of nucleators such as the actin-related protein 2/3 (Arp2/3) complex (Higgs and Pollard, 2000). Disassembly, by contrast, is believed to be enhanced by myosin activity, although dedicated severing proteins also exist (Blanchoin et al., 2000); suppression of myosin activity has been implicated in reduced actin turnover in a range of cellular contexts (Guha et al., 2005; Medeiros et al., 2006; Murthy and Wadsworth, 2005; Yang et al., 2012).

Owing to the complexity of cellular environments, *in vitro* experiments are more amenable to direct observation of myosin-II-driven severing of actin filaments (Haviv et al., 2008; Murrell and Gardel, 2012; Vogel et al., 2013) and network disassembly (Reymann et al., 2012). Although various reconstitution studies have addressed the mesoscopic effects of myosin contractility on actin network reorganization, a direct investigation of the role of myosin in network turnover has been lacking. The observation of actin turnover has previously been limited either by factors such as stabilized actin filaments, diffusion constraints and restricted polymerization (Köster et al., 2016; Linsmeier et al., 2016; Murrell and Gardel, 2012; Smith et al., 2007; Stam et al., 2017; Vogel et al., 2017, 2013) or by a focus on macroscopic network-level changes rather than individual network components (Carvalho et al., 2013; Soares e Silva et al., 2011; Köhler et al., 2011; Bussonnier et al., 2014).

By reconstituting a biomimetic actin cortex where assembly and disassembly coexist and restraints on the mobility of components are minimized, we demonstrate that myosin-II activity can generate turnover in membrane-associated branched actin networks. Qualitative attributes of the contraction process are shared with previous studies, but our minimal cortex additionally shows redistribution of network components after disassembly of actin and recruitment of the released components into new assembly – the key features of actin network turnover.

RESULTS

Assembly of a dynamic actomyosin cortex on supported lipid bilayers

For the reconstitution of a biomimetic minimal cortex with the potential for actin network turnover, we required a strong catalyst of actin polymerization to oppose myosin-driven disassembly. The constitutively active version of murine N-Wasp, also known as VCA

(verpolin homology, cofilin, and acidic domain), served as the catalyst. VCA was anchored to a supported lipid bilayer (SLB) with the stable association of a 10× histidine tag to nickelated lipids (Nye and Groves, 2008). Not only does the membrane localization of the catalyst emulate the cellular scenario, but it also allows preferential imaging of the polymerization process using total internal reflection fluorescence (TIRF) microscopy, which only illuminates a depth of roughly 100 nm into the sample. VCA has been extensively studied *in vitro* and has been shown to promote the autocatalytic growth of a branched actin network when combined with the Arp2/3 complex (Machesky et al., 1999; Pantaloni et al., 2000; Rohatgi et al., 1999). Such ‘dendritic’ network assembly is fast and, therefore, a suitable choice for counterbalancing disassembly by myosin activity. Muscle myosin-II motors were preassembled into filaments and introduced into the system after actin assembly (Fig. 1A).

We started with the characterization of actin assembly in the absence of myosin motors. After a short time lag, surface actin intensity rapidly increased on the VCA-functionalized SLBs in the presence of Arp2/3 and actin monomers (Fig. 1B; fit data in Table S1, Movie 1). The observed time profiles are characteristic of the autocatalytic nature of dendritic actin network assembly (Machesky et al., 1999; Pantaloni et al., 2000). Actin network growth was dense and a bundle-like organization of filaments emerged with time, possibly caused by the spontaneous alignment of actin filaments in close packing (Fig. 1C). Actin assembly was significantly weaker when Arp2/3 was excluded from the reaction and nearly non-existent in the absence of VCA (Fig. 1B). Although VCA alone was sufficient to induce some actin assembly, the resulting meshwork was coarser than in the presence of Arp2/3 (Fig. S1A). This Arp2/3-independent assembly can be attributed to the ability of VCA to enhance actin filament elongation on surfaces by increasing the local availability of monomers (Bieling et al., 2018). By contrast, Arp2/3 alone failed to initiate any actin polymerization on the membrane (Fig. 1B, Fig. S1A). VCA not only activates the Arp2/3 complex, but is also necessary to mediate actin–membrane interactions in this minimal cortex; consequently, adding VCA to this sample immediately led to increased actin intensity on the surface and initiation of filament assembly (Fig. S1A). Together, these trends confirm that the actin assembly we observed on the membrane is dependent on VCA, with considerable contribution from Arp2/3-induced branching.

In contrast to previous studies using a related nucleation promoting factor (NPF) adsorbed on glass (Reymann et al., 2010), the diffusional mobility of VCA on the membrane (Fig. S1B) appeared to be essential for the actin network growth observed in our experiments, as holes in the lipid bilayer were largely devoid of actin, even though VCA accumulated there (Fig. S1C). VCA intensity on the membrane remained stable during actin assembly (Fig. S1D, Movie 1). Actin was grown for 1.5–2 h before the addition of myofilaments, with the aim of maximizing the incorporation of actin monomers into a dense network, thereby reducing the effect of sample-to-sample variation in actin growth profiles (Fig. S1E, Table S2) on the myosin experiments.

Introducing myosin-II to the dendritic actin network resulted in condensation of actin into contraction foci. Interestingly, two distinct length scales of actomyosin contraction were observed under identical experimental conditions (Fig. 1D, Movie 2). In nearly half of the samples ($n=24$), the contraction foci were distributed homogeneously with shorter distances between them ($9.1\pm 2.2\ \mu\text{m}$, mean \pm s.d.) and actin enrichment in these foci was less pronounced. In the remaining samples, we observed a distinct coarsening process, with actin condensing into dense foci separated by larger length scales ($20.3\pm 7.4\ \mu\text{m}$). The characteristic length

scales of the two contraction modes were calculated as nearest neighbor distances of the contraction foci (Fig. 1E).

The bimodal outcome of contraction led us to investigate the factors that impact the length scale of contraction in membrane-associated dendritic actin networks. We found that this length scale responded to manipulations of the surface density of VCA, Arp2/3 concentration, myosin concentration and branch capping (Fig. S2). A fivefold increase in VCA surface density, leading to a net increase in membrane attachment of the actin network, reduced the length scale by one-third (Fig. S2A). Furthermore, enhanced branching resulting from increased Arp2/3 concentrations trended toward the lower length scale (Fig. S2B). Lower myosin concentrations and the introduction of branch capping, presumably resulting in shorter filament lengths, also favored lower length scales (Fig. S2C,D). These dependencies corroborate a previous *in vitro* study, in which membrane adhesion and filament crosslinking were shown to affect contraction length scale in a disordered actin network (Murrell and Gardel, 2012).

Although TIRF illumination only revealed the organization of actin in approximately 100 nm of the few microns that the network can extend from the membrane (Fig. S3A), maximum intensity projections of z -stacks acquired by spinning disk confocal microscopy showed contraction modes similar to those seen in the TIRF micrographs (Fig. S3B, cf. Fig. 1E). This indicates that the actin intensity changes observed on the membrane are reflective of the density changes in the total thickness of the actin network. Furthermore, reduced photo-induced damage of the actin network even at high temporal resolutions make TIRF microscopy suitable for analysis of this reconstituted actomyosin cortex.

Myosin-II breaks down membrane-associated actin networks

Irrespective of the length scale of contraction, we found that myosin activity led to disassembly of the actin cortex (Fig. 2). The initial stages of myosin contraction showed bundling of actin filaments (Fig. 2Aa, white arrows; Movie 3). This was followed by compaction of the actin into contraction foci, resulting in rips in the actin network. Finally, this process resulted in a decrease in actin intensity on the surface, indicating network breakdown. Myofilaments were associated with bundles as well as condensed actin foci (Fig. 2Ab, yellow arrows). Myofilaments, however, accumulated on the membrane while the actin intensity dropped with disassembly (Fig. 2B). By contrast, the surface density of myosin did not increase in the absence of actin on the membrane (Fig. S3C).

The length scale of the rips in the actin network determined whether the mode of contraction was homogeneous or coarse, with larger rips observed in the latter case. In both cases, actin intensity on the membrane reduced by 50% within 5 ± 1.7 min of addition of myosin (Fig. S3D). The contraction events were myosin-specific and required a continuous supply of ATP, as the process stalled at the bundling stage in the absence of ATP regeneration (Movie 4). Because myosin continues to bind actin in the absence of ATP, rapid disintegration of the bundles was observed once new ATP was made available by supplying ATP regeneration mix.

The dense actin condensates formed during coarsening allowed distinct observation of actin filament breakdown upon contraction. Representative images and a kymograph of one of these foci illustrate the disassembly of actin filaments in the core after condensation (Fig. 2C). By following the individual radial profiles of actin and myosin intensities in these foci at different time points, we observed that the condensation process was followed by hollowing of the foci (Fig. 2D). The actin intensity at the core decreased drastically, whereas myosin intensity showed a comparatively minor reduction

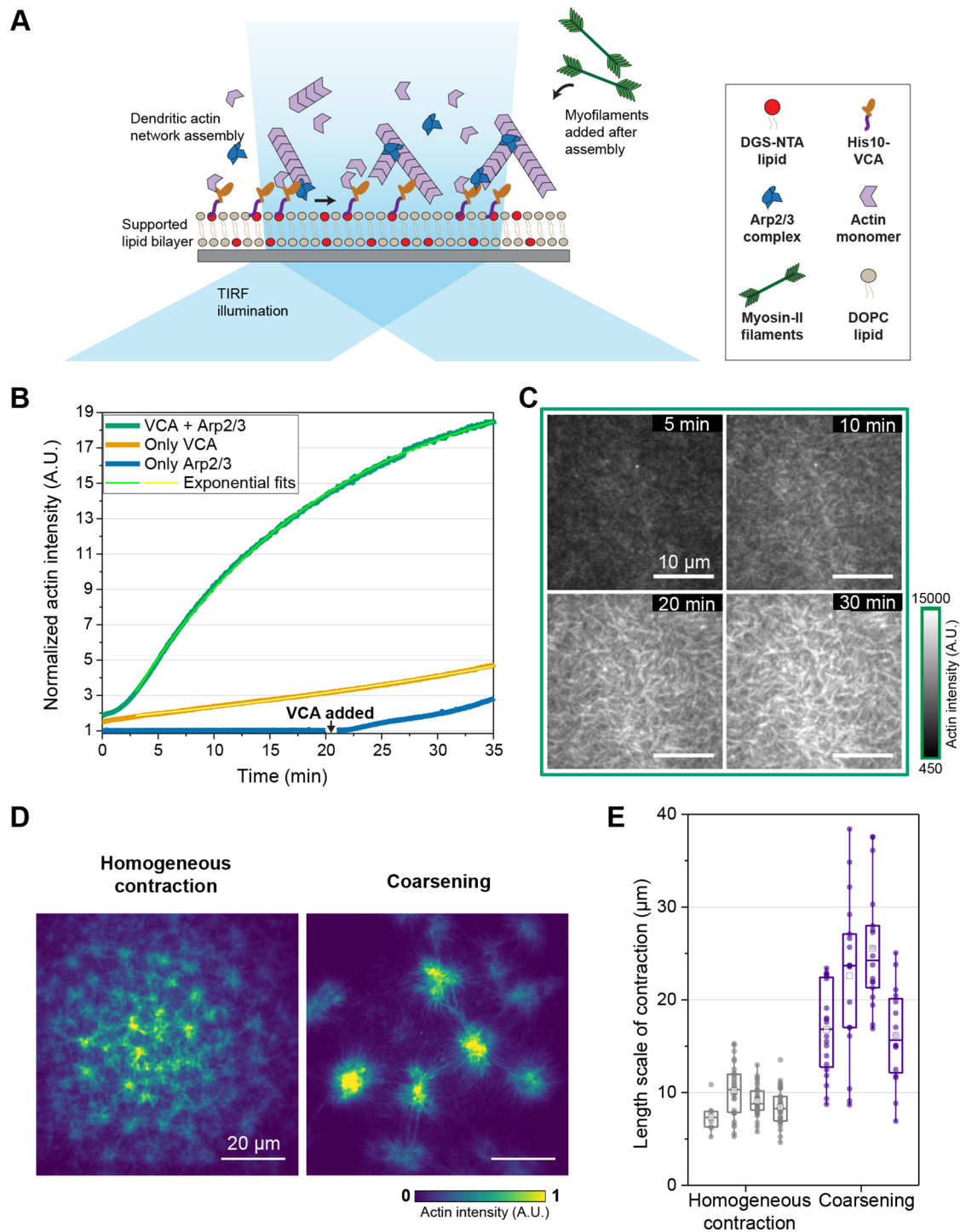


Fig. 1. Assembly of a dynamic actomyosin cortex on supported lipid bilayers. (A) Design of a minimal dynamic actomyosin cortex. A dendritic actin network is assembled on a supported lipid bilayer by Arp2/3-induced branch nucleation, catalyzed by VCA anchored to nickelated lipids (DGS-NTA). Myofilaments are introduced after actin assembly and the system is observed using TIRF microscopy. (B) Time profiles of actin assembly on the membrane and its dependence on different reaction components. Growth was slower in the absence of Arp2/3 and undetectable in the absence of VCA. Addition of VCA (arrow) to the latter resulted in an immediate increase in actin intensity. Concentrations used were 1 μM actin, 10 nM Arp2/3 complex and 100 μM ATP on an SLB with 1 mol% DGS-NTA. Actin intensity was normalized to the value measured before the reaction was triggered by adding the G-to-F buffer. Fit parameters are provided in Table S1. (C) Time frames from the profile of the VCA+Arp2/3 reaction depicted in B. Time is measured from mixing of the reaction components. Images of control conditions are provided in Fig. S1. (D) Representative images of the two modes of actomyosin contraction observed when 0.8 μM myosin-II was added to actin assembled by the VCA+Arp2/3 reaction in B. The two modes were observed under our standard experimental conditions with a 50% likelihood (13 out of 24 samples showed coarsening). The modes differed in density and distribution of condensates. (E) Characteristic length scale of contraction was calculated as nearest neighbor distance between foci. Plot shows the 25–75 percentile as a box, range within 1.5 interquartile region as whiskers, median as a line and mean as a square. Individual data points representing pairwise distances between foci are depicted as closed circles. Each data set represents an individual sample. Length scales were significantly different between the two modes ($P < 0.05$; Mann–Whitney U test).

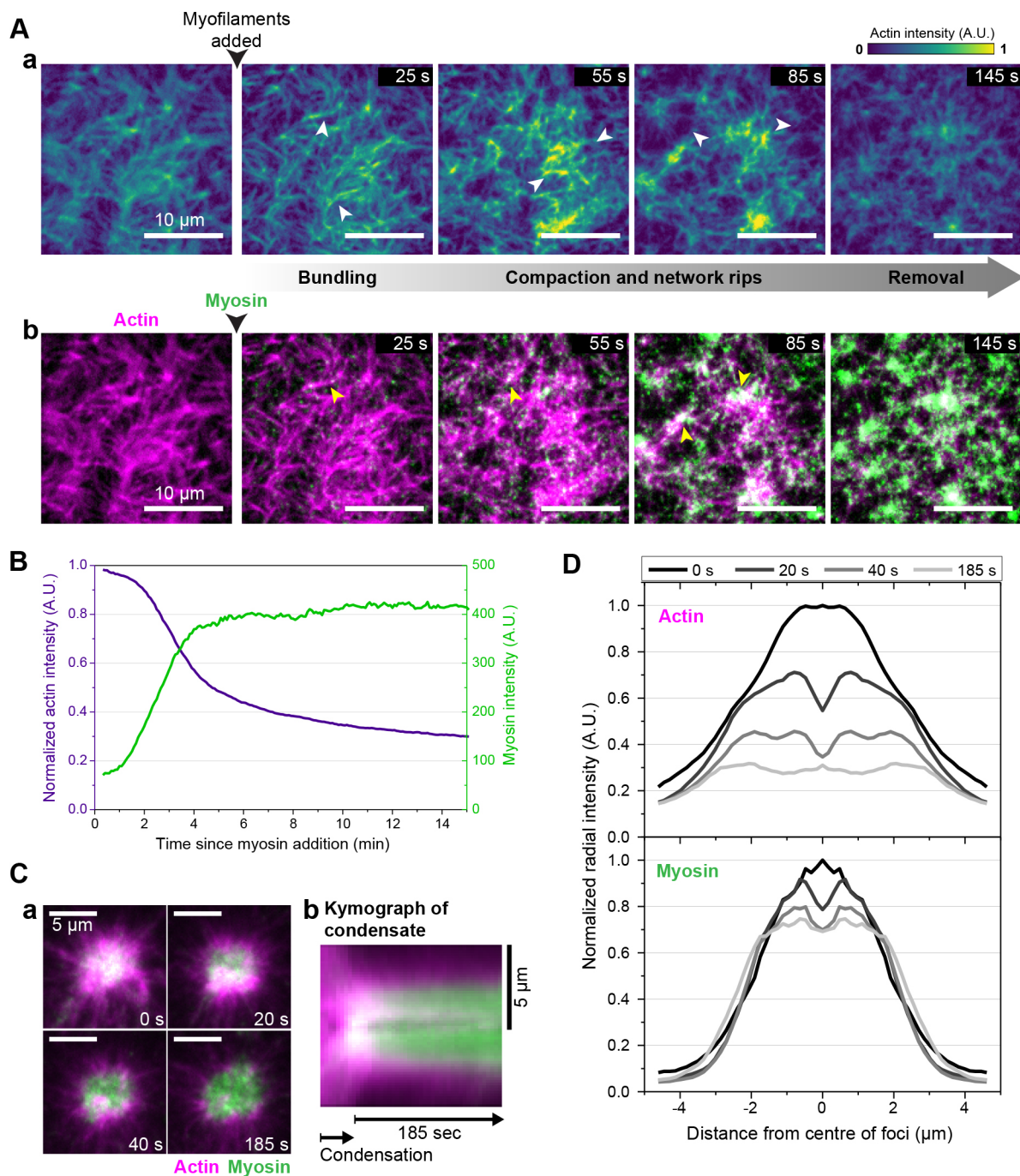


Fig. 2. Myosin-II breaks down membrane-associated actin networks. (A) (a) After addition of myofilaments, dendritic actin networks showed bundling, compaction and network rips (white arrows) and, finally, removal of actin from the membrane. (b) Location of myofilaments (green) in the corresponding frames of panel a. Yellow arrows indicate myosin in actin bundles and foci. Time since the addition of myosin is given in seconds. Images are background subtracted. (B) Time profiles of actin and myosin intensities from the sample described in A. The actin intensity was normalized to the value before addition of myosin and decreased as the myosin intensity on the surface increased. Additional myosin profiles are provided in Fig. S3C ($n=3$). (C) Selected time frames from TIRF imaging (a) and kymograph (b) depicting the release of actin from a single condensate formed during coarsening. The kymograph shows intensities averaged over a 10-pixel thick vertical line through the center of the condensate. Time is measured from the maximum compaction of the condensate. Data is representative of ten condensates from three samples. (D) Radially integrated intensities of actin and myosin at the different time points depicted in C, showing hollowing of the actin core and reduction in actin in the foci. The decrease in myosin intensity was less pronounced over the same time period.

(Fig. 2Cb,D). This indicates that the actin filaments disintegrate rapidly under the stresses generated by the enriched myosin motors as contraction continues in the condensed actin foci.

Individual events of filament fragmentation were difficult to observe in the dense network. However, as actin condensed into coarser foci, bundles of actin were observed distinctly linking the

foci. As contraction proceeded, these bundles ruptured abruptly and recoiled, revealing the tensile stresses acting on them (Fig. S3Ea,b). Myofilaments could be seen as distinct puncta along the bundles, presumably crosslinking the actin filaments (Fig. S3Ec). This explicitly shows one mode of filament breakage caused by contraction in the dendritic network.

Redistribution in active networks restores a homogeneous actin distribution

The stark changes in actin distribution generated during coarsening also enabled us to observe phenomena that were not discernable during homogeneous contraction. Although coarsening initially generated a very heterogeneous actin distribution on the membrane, the actin network eventually resumed a seemingly uniform organization (Movie 5). In Fig. 3A, the coefficient of variation (CV) of the intensity distribution of actin is used as an indicator of the heterogeneity of its physical distribution on the membrane. The CV was calculated as the ratio of standard deviation to the mean of the actin intensity distribution at each time point. The increase in CV coincided with the contraction process upon addition of myofilaments, peaking with coarsening (Fig. 3Aa–c). The CV then dropped as the actin was redistributed and, finally, the actin distribution was nearly as homogeneous as before the addition of myosin (Fig. 3Ad–f, graph). This observation suggests that large-scale heterogeneity in actin distribution is unstable in this dynamic minimal cortex and that network reorganization continues until a more homogeneous actin distribution is achieved. The resulting distribution was similar to that observed when contraction proceeded homogeneously (Fig. 3A, graph).

The restored uniformity in actin distribution can be attributed to two phenomena that occur simultaneously: the loss of actin from contraction foci and the recovery of actin filaments on the remaining regions of the membrane (Fig. S4A). The loss of actin resulted from breakdown of condensed actin in the foci, as described in the previous result (Fig. 2D) and also observable in Fig. 3Ac,d. The concomitant reappearance of actin in other regions was accompanied by formation of new myosin foci in these parts (Fig. 3Ba, white arrows; Movie 6). A kymograph of a stretch between two contraction foci revealed that both actin and myosin contributed to the newly emerging node (Fig. 3Bb,c). Myosin intensity, however, increased with a slight delay after actin intensity in the new foci (Fig. 3Bc, inset), suggesting that actin drives the reorganization. This delay was variable between nodes, ranging from 5 to 40 s. The source of the material for the new foci cannot be distinctly discerned, but both actin and myosin were exchanged with the neighboring foci (Fig. 3Bb, white arrows; Movie 6). Myosin accumulated in the new foci with time, whereas actin intensity remained constant (Fig. 3Bb,c). These observations indicate that, although myofilaments largely follow actin filaments, the former appear to become restrained once they reach the foci, even though actin is exchanged between the foci without any net retention.

As expected, this reorganization resulted in a reduction in the distances between foci, which we previously measured as contraction length scale during coarsening (Fig. 3Ca,b). The final values approached the length scale of homogeneous contraction (Fig. 3Cb), indicating that for a given set of experimental conditions the actomyosin network has a favored length scale that is restored in spite of initial disturbances.

Unlike myosin, VCA localization on the membrane was stable during contraction (Fig. S4B) and unaffected by coarsening (Fig. S4C), suggesting that VCA-driven actin polymerization could contribute to the reappearance of actin during redistribution. Interestingly, VCA was also enriched in the late-stage actomyosin foci formed on the membrane, possibly enhancing polymerization at these sites (Fig. S4C). However, although redistribution of actin resulted in a local increase in actin intensity, mean actin intensity on the entire membrane did not increase after the initial reduction during contraction (Fig. S4D). Thus, a considerable proportion of the actin network was permanently lost from the membrane, coinciding with the appearance of condensates in solution

(Fig. S4Ea), reminiscent of previous solution studies (Soares e Silva et al., 2011). The shape dynamics of these condensates indicate that myosin is active in them (Fig. S4Eb), possibly trapping the actin filaments by crosslinking and recapture.

A dynamic steady state actin distribution emerges in the minimal cortex

Image cross-correlation analysis showed that the myosin-driven redistribution of actin on the membrane ultimately resulted in the emergence of a dynamic steady state, wherein the actin distribution remained fairly constant. The actin fluorescence signal in each frame of the time series was cross-correlated with the first frame of the series, thereby using the actin distribution before addition of myosin as a fixed reference for estimating changes in actin distribution at different time points. As expected, the correlation coefficient dropped sharply during the initial disassembly of the actin network, when massive changes in network organization took place. At later time points, however, the correlation coefficient stabilized at approximately 0.8, indicating the emergence of a new, steady state actin distribution that was similar, but not identical, to the actin distribution before addition of myosin (Fig. 4A). The similarity probably stems from the restored homogeneity in actin distribution (see Fig. 3A), which also remained stable for the ~45 min duration of observation (Fig. S5A). The mean actin intensity showed a slight reduction for another 15–20 min before stabilizing (Fig. S5A), suggesting that the steady state actin distribution is maintained even if there is some loss of actin at the membrane. Interestingly, this steady state distribution emerged irrespective of whether the initial contraction proceeded through coarsening or homogeneous contraction of the network (Fig. 4A).

It is important to note that the actin network was still dynamic in the steady state, as actin bundles between the late-stage foci continued to show restructuring (Movie 7, Fig. S5B). To investigate this further, we cross-correlated the actin signal in each frame of the time series with the frame 25 s ahead (five frames ahead), thus estimating how similar the actin distribution remained over this fixed time interval (Fig. 4B). The correlation coefficient again showed an initial drop during disassembly of the actin network. During the steady state (after 15 min), the correlation coefficient stabilized at approximately 0.8, indicating minor reorganization within the chosen time window of 25 s. The value below 1 and the fluctuations show that the steady state was indeed dynamic. Longer time windows also showed a stable average correlation coefficient of 0.8, indicating that no large-scale changes to the actin distribution occurred on these times scales and that the relevant time scale for reorganization within the dynamic steady state was less than 50 s (Fig. 4B, inset).

The flows of actin that persist between the stably distributed late-stage foci can also be visualized in the form of vector maps, in which each vector depicts the spatiotemporal intensity gradient calculated over five frames, amounting to a time period of 25 s (Fig. 4C, middle rows). Comparing these images at three different time points on the curve in Fig. 4B shows the flow of actin at different stages. Although hardly any dynamics were observed in the actin network before the addition of myosin (Fig. 4Ca), the actin flowed into large condensates during coarsening (Fig. 4Cb). In the later steady state, actin flows were higher in the vicinity of the late-stage foci (Fig. 4Cc). The dynamics are further illustrated by color-coded maps of pixel-wise intensity gradients calculated between the image at the selected time t and the image at time $t+25$ s (five frames ahead). In these maps, actin intensity reduced in the blue regions as it increased in the red regions. The red regions again coincided with

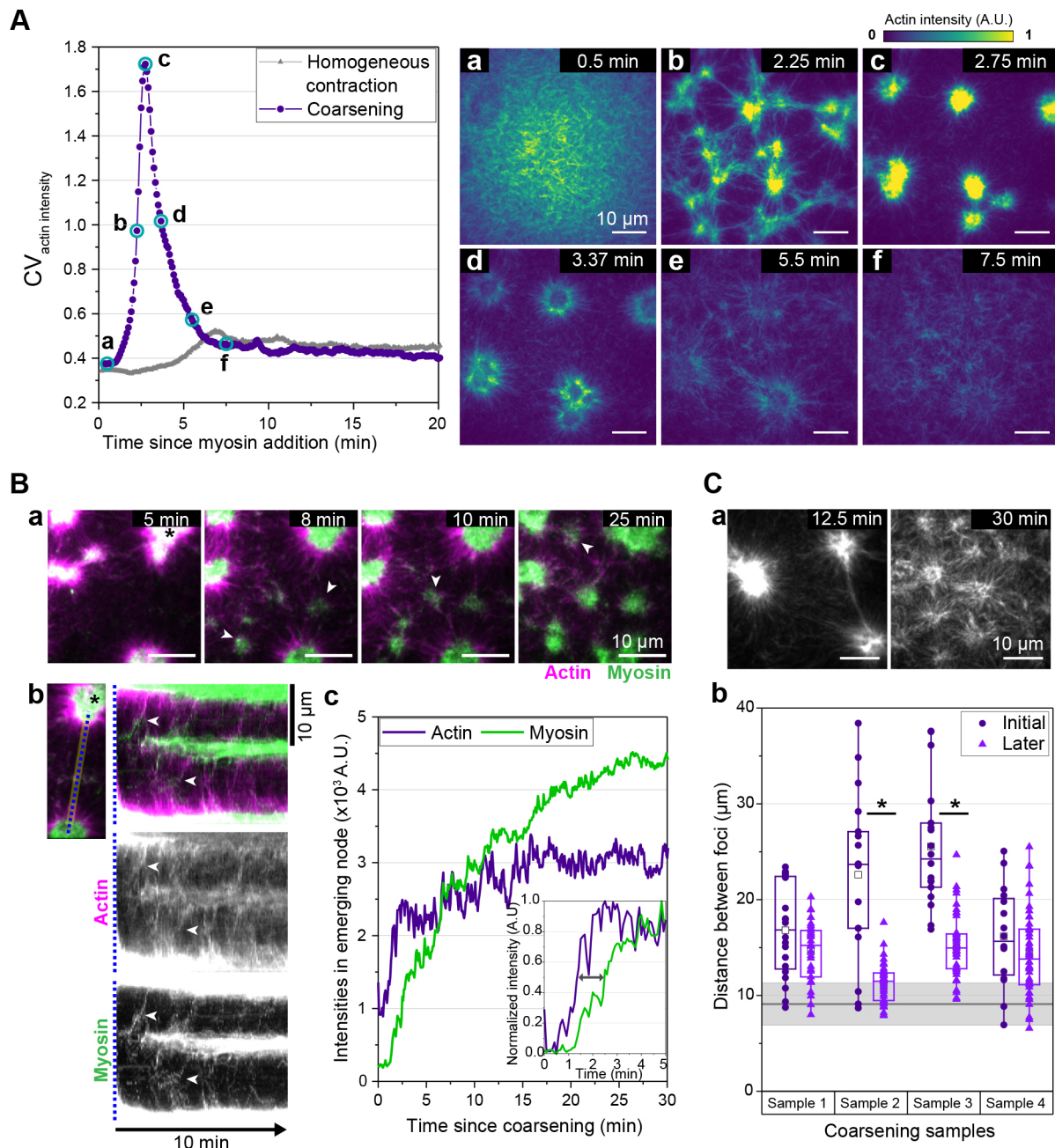


Fig. 3. Redistribution in active networks restores homogeneous length scales. (A) Heterogeneity of actin distribution during contraction is represented by the CV of actin intensity in the image plotted over time. CV is calculated as the standard deviation divided by the mean of the actin intensity distribution for each time frame. Images corresponding to the time points highlighted by cyan circles in the profile of coarsening are shown on the right (a–f). Data is representative of three samples each for coarsening and homogeneous contraction. (B) (a) The reappearance of actomyosin foci in regions where actin was removed during coarsening is indicated by white arrows in selected time frames. Time since the addition of myosin is depicted in minutes. (b) The kymograph plotted from a 10-pixel thick line connecting two foci shows the emergence of new foci in between. White arrows indicate transfer of material between the foci. Actin and myosin are individually shown in grayscale in the lower frames. (c) The graph shows actin and myosin intensity changes in the newly emerging node measured in a circular region of 10-pixel diameter. Time is measured from the point of maximum compaction during coarsening. The graph inset shows normalized intensities in the first 5 min as the new foci emerges, with the time gap at half-maxima indicated by the arrow. Data is representative of 32 nodes from 3 independent samples. (C) (a) Representative images of the transition of actin distribution in a sample. Time since myosin addition is indicated. (b) In samples showing coarsening, the distance between neighboring foci decreased over time, coming closer to the value of length scale of homogeneous contraction (gray line with the shaded area depicts mean \pm s.d.). Plot shows the 25–75 percentile as a box, range within 1.5 interquartile region as whiskers, median as a line and mean as a square. Individual data points are depicted as closed circles or triangles. The length scales were calculated at the peak of coarsening (Initial) and then again approximately 20 min after the addition of myosin (Later). Asterisks indicates samples where differences are significant after transition ($*P < 0.05$; Mann–Whitney U test).

the foci, interspersed with regions of blue between them, suggesting that actin flows into the foci from the surrounding regions.

Together, these analyses demonstrate that actin distribution on the membrane achieved a dynamic steady state that was observed for

up to 1.5 h after the introduction of myosin (Fig. S5B). The emergence of a steady state actin distribution could indicate that the opposing processes of actin polymerization and myosin-driven disassembly counterbalance each other in this minimal cortex.

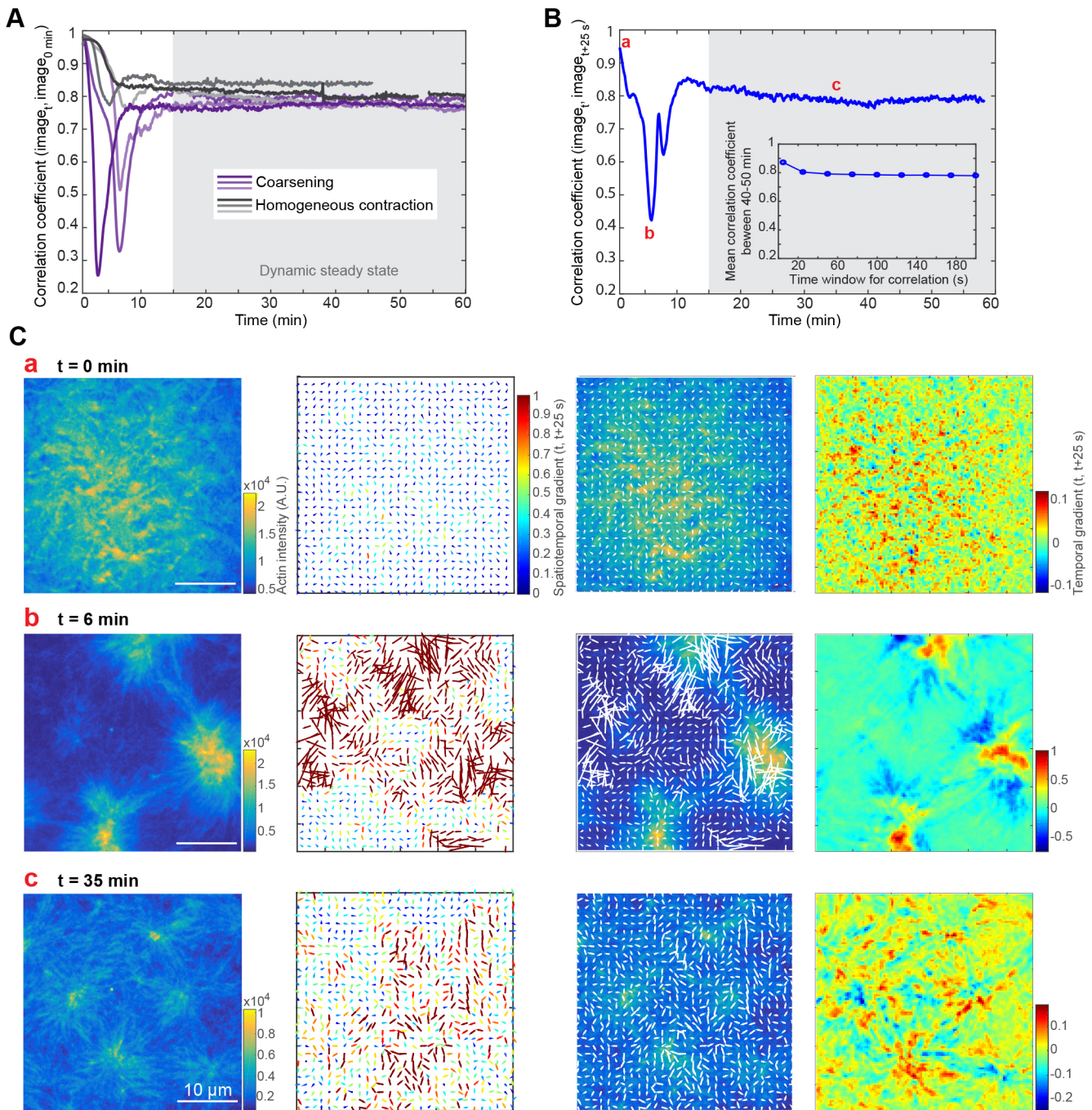


Fig. 4. Image cross-correlation analysis reveals the emergence of a dynamic steady state actin distribution in the minimal cortex.

(A) Correlation coefficient calculated by cross-correlating the actin fluorescence signal from each frame with the first frame of the time series, i.e., with the actin distribution before myosin was added (increasing time window, fixed reference frame). A correlation coefficient close to 1 indicates a high similarity of the frame with the initial image; comparing two random images would give a correlation coefficient of 0. Three samples each show coarsening (purple) or homogeneous contraction (gray). The region between 15 and 60 min is shaded gray to denote the period in which the correlation coefficient is stable at approximately 0.8 (i.e., the steady state). (B) Correlation coefficient along the time series for the correlation of each frame with the frame 25 s ahead (constant time window, moving reference frame), calculated for a coarsening sample. This correlation coefficient indicates the self-similarity of the actin distribution with a time window of 25 s. The inset shows a plot of the mean of the correlation coefficient over 10 min during the steady state for different time windows. The period between 40 and 50 min was selected as a representative time period within the steady state regime. Three time points (a, b, c) were selected for further analysis (shown in C). Movie 7 shows the actin dynamics observed during the steady state. (C) Panels show the actin distribution (upper row) before the addition of myosin (a), at the peak of coarsening (b) and during the dynamic steady state (c). All other rows show analysis of actin flows at the same time points. The second row from the top shows a vector map of the spatiotemporal gradient of intensity calculated for a time window of 25 s (five frames). The arrows are color-coded for the absolute value of the spatiotemporal gradient of intensity. The third row shows an overlay of the spatiotemporal gradient map on the actin intensity image. The bottom row visualizes the pixel-wise temporal gradient of the intensity, which is simply given by the difference of the image at the selected time point and the image 25 s ahead. Positive values indicate an increase in intensity and negative a decrease. Data is representative of the analysis from three coarsening samples.

However, the steady state could also result from mere shuttling of actin filaments on the membrane by myosin motors in the absence of any new actin polymerization. The experiments in the following section aimed to examine these possibilities by probing whether monomers from solution are incorporated into the actin network on the membrane in the presence of myosin activity.

Actin network undergoes continuous turnover in the dynamic steady state

To determine whether the pool of actin monomers contributing to the network on the membrane undergoes turnover, we designed a pulse-chase experiment using two differently labeled actin monomers (Fig. 5A). The actin network was assembled as usual with 10% Alexa Fluor 568-labeled actin (Label1). Excess monomers in solution were then removed by extensive washing. Along with myofilaments, additional actin monomers (1 μM) were added to the system, 10% of which were labeled with Alexa Fluor

488 (Label2). Additional Arp2/3 complex (10 nM) was also provided so that the process of reassembly was not limited by its availability. We then looked for the mixing of labels in the actin network on the membrane.

We found that once the Label1 network was disassembled, Label2 in the membrane-associated actin increased steadily after an initial lag (Fig. 5B, graph). The increase in Label2 intensity was accompanied by a gradual decay in Label1 intensity, suggesting that Label2 replaces Label1 in the pool of actin observed on the membrane. As in previous experiments, a stable distribution of foci appeared after the initial reorganization, although the different photophysical properties of the two fluorophores meant that we could not ascertain whether the total amount of membrane actin was conserved. Actin bundles associated with the foci showed a uniform distribution of Label1, interspersed with speckles of Label2 (Fig. 5B, images). Although we could not resolve monomer mixing within individual actin filaments in our images, these results confirm that the two different pools of actin

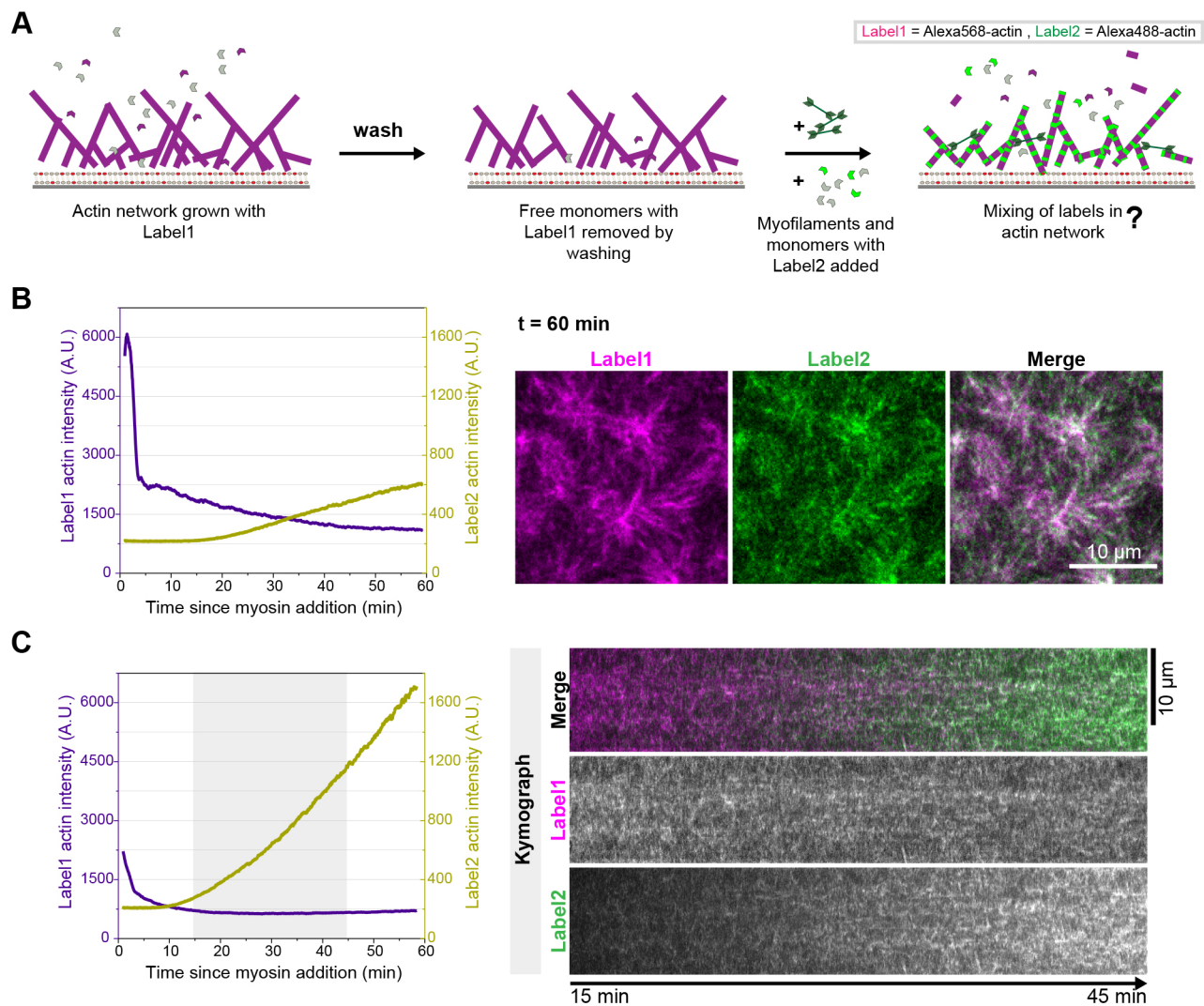


Fig. 5. Actin network undergoes continuous turnover in the minimal dynamic cortex. (A) Experimental design for following the turnover of actin filaments observed on the membrane after myosin contraction. 1 μM of 10% labeled (Label2) actin monomers and 10 nM Arp2/3 were added along with the usual 0.8 μM of myosin. Data from three repeats are compiled in Fig. S5C. (B) The left panel shows a plot of intensity profiles of Label1 and Label2 for one experiment as described in A. The right panel shows the corresponding images at the indicated time point for the same sample. (C) Intensity profiles from a second experiment in which the starting density of the Label1 network was lower. There is a sharper Label2 increase. Right panel shows a kymograph of the time period shaded with gray in the graph, with the Label1 and Label2 profiles separately shown in grayscale.

mix in the membrane-associated actin network in the presence of myosin activity.

If label mixing reflects actin network turnover in the dynamic steady state, Label2 should continue to increase in the actin on the membrane, eventually showing homogeneous labeling. However, the intensity of Label2 increased so slowly that the speckled distribution was still observed after 1.5 h (Fig. S5C,D). Because prolonged imaging increases the risk of phototoxicity and evaporation in our assays, we instead reduced the initial density of Label1 actin by growing it for less than 1 h before washing off excess monomers. The resulting higher ratio of Label2 to Label1 actin in the assay accelerated the kinetics of Label2 incorporation, showing both a shorter initial lag and a faster increase in Label2 on the surface (Fig. 5C, graph). A steady enrichment of Label2 was observed in the composition of the actin network (Fig. 5C, kymograph). The altered initial actin density in this experiment presumably affected other dynamics of the assay, as Label1 intensity did not continuously reduce after the initial sharp fall, even as Label2 increased. Nevertheless, as anticipated, the Label2 distribution in the actin structures on the membrane became more homogeneous with time (Fig. S5E).

The changing composition of the actin network indicates that we did not simply observe the translocation of actin filaments on the membrane by myosin motors during the dynamic steady state; new actin was continuously incorporated into the membrane-associated network in the presence of myosin. Buckling and rupture of actin bundles was observed even 1 h after myosin addition (Movie 8), indicating that disassembly by myosin occurred alongside actin assembly and presumably supported turnover in the network. Actin structures with mixed, interspersed labeling could assemble by one of two mechanisms or through a combination of both: (1) by annealing of actin fragments of different labels, either spontaneously (Murphy et al., 1988) or mediated by multivalent interactions with myosin, or (2) by new filament polymerization with monomers of both labels. The latter mechanism is only possible if Label1 monomers were released from the pre-assembled network upon myosin contraction, because free monomers were washed off before myosin was added. Irrespective of the mechanism involved, our results affirm that the actin released by myosin activity can co-assemble with new monomers on the membrane. Furthermore, the continuous turnover of the actin network on the membrane reinforces the dynamic aspect of the steady state actin distribution.

Disassembly by myosin generates actin turnover in the minimal cortex

Seeking a better understanding of the mechanisms of assembly and disassembly contributing to the dynamic steady state, we systematically perturbed the two main aspects of this reconstituted system in separate experiments: (1) myosin-driven disassembly and (2) VCA-mediated polymerization.

To probe whether the network components released during myosin contraction can be reused for new polymerization on the membrane, we used the myosin-II inhibitor blebbistatin to block myosin activity at a desired stage of actin network reorganization. For this, we again washed off excess monomers from the assembled actin network before adding myosin. After the initial fragmentation and redistribution of actin had taken place, actin growth was allowed to proceed unrestrained by inhibiting myosin-II activity with blebbistatin. Any polymerization observed after myosin activity could only result from the filament fragments and monomers generated by disassembly of the pre-existing actin network.

Together with blebbistatin, actin monomers with a different label were also introduced so that the polymerization resulting from components of the disassembled Label1 actin network could be contrasted with the polymerization of freely available Label2 monomers. In control experiments, blebbistatin was added before myosin could break down the Label1 actin network (i.e., as soon as initial signs of myosin activity such as bundling were observed). In this case, any new assembly of Label1 could only result from monomers generated by the inherent, myosin-independent depolymerization of actin.

We found that when myosin was inactivated after actin network breakdown, the surface intensities of both Label1 and Label2 actin gradually increased, indicating that both fractions of actin were available for new assembly (Fig. 6A). Note that because blebbistatin interferes with the binding of myosin to actin, this increase in intensity was not caused by recapture of actin fragments by myosin, but by actin assembly mechanisms of polymerization and/or fragment annealing. In sharp contrast, if myosin was inactivated before disassembly of the Label1 actin network, the intensity of Label1 merely decreased from photobleaching (Fig. 6B), suggesting that Label1 actin has no significant turnover without myosin activity. Note that this decrease was clearly distinguishable from myosin-driven breakdown, because the pattern of actin distribution on the membrane remained unchanged as the amplitude of its fluorescence intensity reduced (Fig. 6B, images). By contrast, Label2 intensity still increased with time, indicating that the polymerization machinery on the membrane was functional, but that Label1 monomers were probably unavailable. The rates of change in these experiments varied widely because the initial density of the Label1 actin network was different between samples, but all trends were consistent (Fig. S6A). Furthermore, the actin on the membrane after 30 min of myosin inhibition revealed a high degree of colocalization of Label1 and Label2 in the case where myosin broke down the Label1 actin network (Fig. 6A, images). By contrast, when the initial actin network was intact, Label2 appeared to be excluded from the denser regions of Label1 (Fig. 6B, images). Importantly, regrowth of the network after myosin inhibition did not require the introduction of additional actin monomers, as trends similar to those of Label1 actin were observed when the experiment was conducted without adding Label2 actin monomers (Fig. S6B). Together, these results suggest that myosin-mediated breakdown facilitates actin turnover by regenerating the network components (potentially both actin filaments and monomers) required for new actin assembly.

These experiments also show that myosin activity maintains an inhibitory effect on actin assembly, as the surface intensity of actin did not increase when myosin activity proceeded without interruption (see Fig. S5A). This negative feedback could result from the continuous breakdown of growing actin by myosin, and could thus give rise to the dynamic steady state. However, the observation that actin assembly took over when myosin was inhibited does not shed light on how assembly occurs in the presence of myosin.

To distinguish between actin polymerization from monomers and annealing of actin fragments in the actomyosin cortex, we used a capping protein (CapZ) that affects these two processes differently. CapZ increases the density of growing dendritic networks by favoring generation of new branches over elongation of pre-existing branches (Akin and Mullins, 2008). End-to-end annealing of actin fragments, by contrast, is slowed down by capping of barbed ends (Andrianantoandro et al., 2001). When 10 nM CapZ was added during the redistribution of actin after myosin contraction, the filament

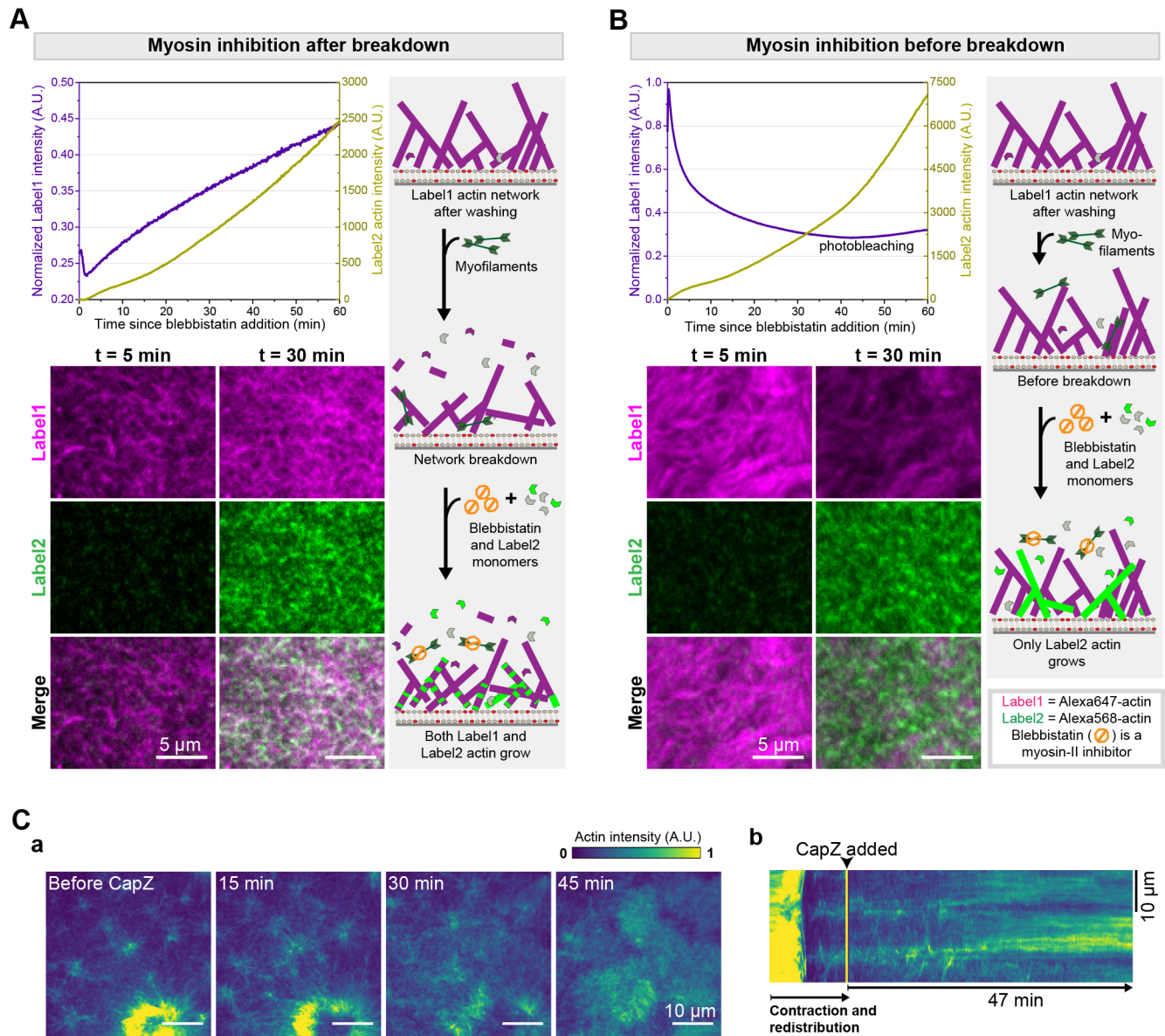


Fig. 6. Myosin-mediated disassembly regenerates network components to facilitate new actin network assembly. (A) Data and schematic of the experiment designed to test whether components released upon breakdown of actin networks by myosin can be used for new actin assembly. Left panel shows the time profiles of Label1 and Label2 intensities when myosin activity is blocked using blebbistatin after the breakdown of the Label1 actin network. Label1 intensity is normalized to the value before the addition of myosin to estimate what fraction of the network recovers after myosin inhibition. Label2 intensities are background subtracted. Lower left panel shows images corresponding to two time points from the graph. Data from all three samples are shown in Fig. S6A. 20 μM of blebbistatin was added for myosin inhibition, along with 1 μM of 10% labeled (Label2) monomers. (B) Time profiles of Label1 and Label2 intensities from the control experiment in which myosin was inhibited before the Label1 actin network could be disassembled. Photobleaching of Label1 is supported by the images corresponding to two time points on the graph. The experiment and outcome are depicted in the schematic on the right. Data from all three samples are shown in Fig. S6A. (C) (a) Time frames showing the change in actin distribution on the membrane when 10 nM of CapZ was added during the redistribution of actin after network breakdown by myosin. Time is measured from the point of addition of CapZ. (b) Kymograph constructed from a line drawn across two contraction foci in the sample shown in panel a. Data is representative of three repeats.

dynamics between the foci were replaced by a denser and more homogeneous actin growth over time (Fig. 6Ca,b). Actin growth was particularly dense in the regions between the foci and markedly low at the foci themselves (Fig. 6Cb, Fig. S6C). Because myosin motors showed an inverted profile of localization, being enriched in the foci (Fig. 2B), it is unlikely that the new actin that appears on the membrane simply results from recapture by myosin. Furthermore, the surface intensity of actin increased even in the presence of myosin (Fig. S6D), potentially because shorter filament lengths interfere with myosin's ability to capture or fragment actin filaments. The increase in

both actin growth and network density in the presence of CapZ indicates that actin polymerization, via a combination of branching and elongation, indeed takes place on the membrane in the presence of myosin activity; it is not solely annealing of actin filaments that maintains the stable actin distribution.

Taken together, these results suggest that myosin-mediated breakdown induces turnover in membrane-associated dendritic actin. Both the processes of actin polymerization and myosin contraction coexist in the minimal cortex, counterbalancing each other to give rise to a dynamic steady state.

DISCUSSION

In this study, we reconstituted a minimal dynamic actin cortex to elucidate myosin-assisted turnover of actin filaments. We employed TIRF microscopy to study the effects of myosin-II contraction on the reorganization of actively polymerizing branched actin networks on membranes. The key distinguishing feature of the minimal actin cortex described in this study is the coexistence of catalytic actin polymerization and the contractile activity of myosin. This enabled us to demonstrate myosin-II-stimulated actin turnover by observing the three main processes of (1) disassembly of pre-existing actin network, (2) redistribution of released network components and (3) reuse of these components for new network assembly (Fig. 7).

Our observations of myosin-driven reorganization of branched actin networks on a membrane are in line with previous studies, which also describe a distinct network coarsening upon myosin addition both in solution (Soares e Silva et al., 2011; Backouche et al., 2006; Köhler et al., 2011) and on membranes (Köster et al., 2016; Linsmeier et al., 2016; Murrell and Gardel, 2012; Smith et al., 2007; Stam et al., 2017; Vogel et al., 2013). However, beyond this condensation process, we further observed the subsequent *de novo* polymerization and redistribution of actin on the membrane (Fig. 7), with only one of the solution studies previously reporting a similar phenomenon of an emergent dynamic steady state (Köhler et al., 2011). This finding highlights the dynamic nature of the minimal actomyosin cortex that we reconstituted.

On a lipid bilayer, fragmentation of individual actin filaments by myofilaments, in isolation or within a dense network, has been demonstrated (Murrell and Gardel, 2012; Vogel et al., 2013).

However, the breakdown and removal of membrane-bound actin after initial compaction was probably impaired by strong membrane adhesion of the biotinylated actin filaments (Vogel et al., 2013) or the use of crowding agents in solution (Murrell and Gardel, 2012). By contrast, in the minimal cortex described here, only the nucleation promoting factor (VCA) was firmly bound to the nickelated lipids in the membrane. The membrane association of actin, resulting from the cumulative effect of multivalent interactions between actin filaments and the VCA, was persistent but dynamic. Our set-up is a reasonable approximation of cellular environments, where proteins linking actin networks to membrane undergo fast turnover (Fritzsche et al., 2014), effectively enabling a highly dynamic association by an alternative mechanism. Such reversible filament anchoring might be crucial for the observed myosin-driven disassembly of dendritic actin networks, as similar processes were reported when actin networks were grown from a related NPF adhered to a glass surface (Reymann et al., 2012). Notably, we observed actin disassembly in the form of a distinct hollowing of actin condensates on the membrane, previously reported only in solution actomyosin aggregates (Soares e Silva et al., 2011). However, in contrast with those observed in solution, these actin shell-like structures were transient on the membrane, presumably because the polymerization machinery enabled further redistribution of actin.

After coarsening, a synergistic relocation of actin and myosin, possibly driven by actin polymerization, led to a more homogeneous distribution of contraction foci. The active network then continued to show long-term flows of actin filaments over this

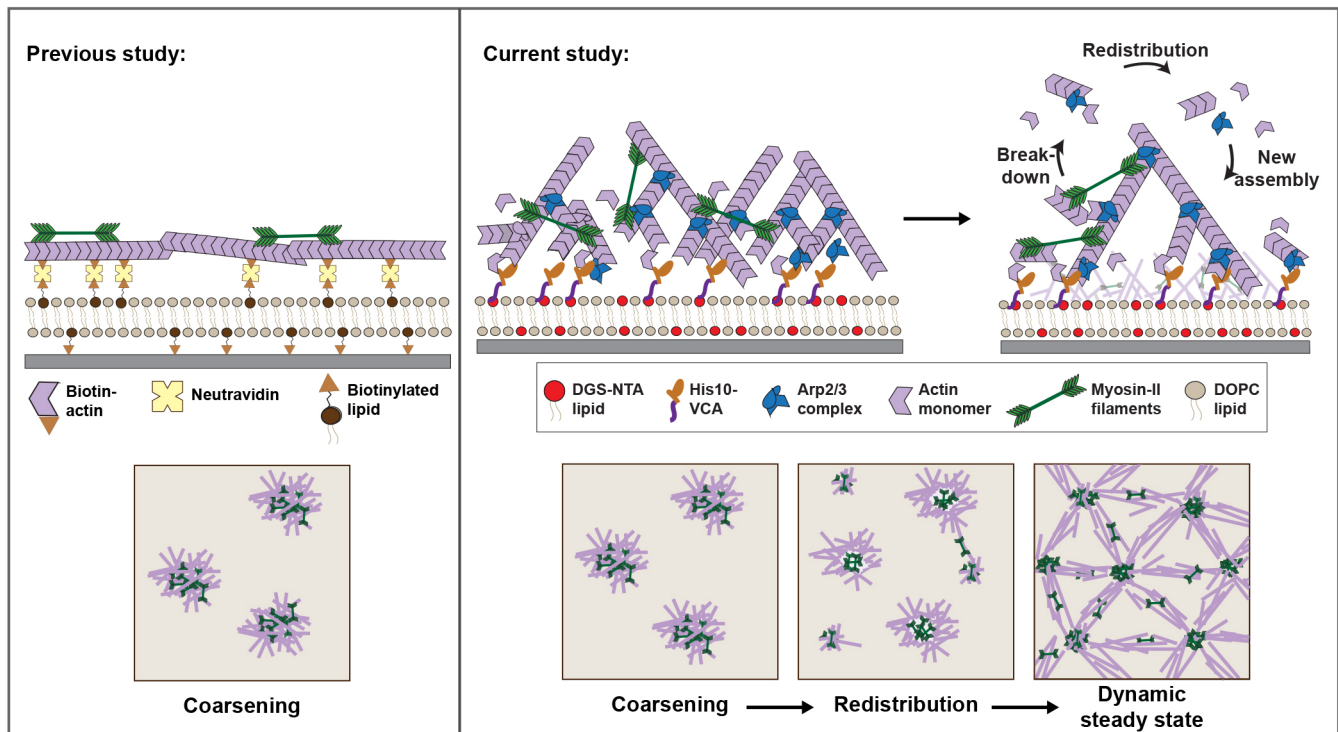


Fig. 7. Myosin activity generates a dynamic steady state actin distribution with continuous turnover in a minimal actin cortex. Schematic comparing the results of our study with a previous reconstitution of a minimal actin cortex, where pre-formed actin filaments were attached to an SLB via neutravidin-mediated bridging of biotinylated actin monomers and biotinylated lipids (Vogel et al., 2013). Our experimental design overcomes constraints on actin assembly and diffusion by using the VCA–Arp2/3 actin filament nucleation module that enables both fast actin polymerization as well as dynamic membrane attachment. Consequently, in the previous study myosin-II-driven reorganization of actin was limited to coarsening, whereas we observed a subsequent redistribution resulting in the emergence of a dynamic steady state actin distribution in our minimal dynamic actin cortex. The three key aspects of actin network turnover are observed in this reconstituted cortex: (1) breakdown of membrane-bound branched actin networks by myosin, (2) redistribution of network components on the membrane and (3) incorporation of these network components in the new actin assembly on the membrane.

preferred length scale, resulting in the emergence of a dynamic steady state actin distribution, previously described only in solution clusters (Köhler et al., 2011). The dramatic reorganization observed when capping of actin filaments was introduced during the redistribution suggests that actin polymerization is higher in the region between contraction foci, whereas myosin-driven disassembly predominates at the foci. Such emergent segregation of actin assembly and disassembly could contribute to the pulsatory dynamics observed during certain developmental processes (Nishikawa et al., 2017; Martin et al., 2009). A compelling avenue for more detailed investigation is to dissect actomyosin organization in the emergent distribution with higher spatial resolution and determine the influence of other structural components of cortical networks. This approach would also shed more light on the regulation of length scales in the reconstituted cortex. We observed a dependence on net membrane association of the actin network, branching densities and possibly filament length and active motor concentration, consistent with previous observations of contraction in disordered actin networks on membranes (Murrell and Gardel, 2012). These are all factors that are subject to extensive biochemical regulation in cell cortices and could, therefore, contribute to the coordination of actomyosin activity over different length scales in a cell.

Finally, we elucidated the contribution of myosin activity in actin filament turnover in this reconstituted cortex. The notion that myosin enhances actin turnover rates has been suggested in various cellular contexts (Guha et al., 2005; Medeiros et al., 2006; Murthy and Wadsworth, 2005; Yang et al., 2012; Wilson et al., 2010), but the inhibition of myosin activity is a fairly complex perturbation because of the many roles of myosin-II motors in the cytoskeleton. In our simplified cortex, by timing myosin inhibition appropriately, we could demonstrate that fragmentation by myosin augments turnover in membrane-associated actin by regenerating network components. Our results with capping of actin filaments suggest that actin polymerization via branching and elongation probably contributes to the actin growth observed during myosin inhibition. Because actin polymerization requires monomers, but free monomers had been washed off in these experiments before adding myosin, the observed actin growth implies that monomers were regenerated from myosin-driven breakdown of the pre-assembled actin network. Fragmentation by myosin might enhance the spontaneous depolymerization of actin filaments by generating more filament ends. Myosin-driven disassembly could thus amplify local cortical remodeling by providing fast access to a pool of network components for new assembly. Because actin organization is coordinated over micron-scale distances in the cell from a limited pool of components, this suggests an interesting mechanism by which myosin activity could support faster dynamics on a shorter length scale.

In this simplified cortex, we selected only the minimal components required for dendritic network assembly and contraction to gain a clearer understanding of the role of each participating component. This might be the reason why actin network turnover appeared to be much slower in the reconstituted cortex than *in vivo* (Fritzsch et al., 2013). In the cell, the dynamics of both assembly and disassembly are augmented by multiple parallel pathways, which make it difficult to analyze the contribution of individual mechanisms in complex processes. The objective of reconstitution techniques is to offer controlled environments, in which intricate manipulation of isolated cellular pathways can be carried out. These advantages enabled us to provide a proof-of-principle demonstration that myosin activity, when counterbalanced by actin polymerization, can induce actin turnover in

a minimal cortex and result in the formation of an active network in dynamic steady state on the membrane. Furthermore, this experimental set-up has the potential to be developed as a paradigm for quantitative analyses of turnover rate, with a few adaptations. Reconstitution could then be used, for instance, to compare the enhancement of actin turnover when cofilin or non-muscle myosin-II drives network disassembly. By virtue of being readily amenable to increased complexity, the dynamic minimal cortex reconstituted in this study offers a promising platform for seeking further insights into the processes that regulate the functioning of its biological inspiration.

MATERIALS AND METHODS

Proteins and other reagents

The VCA domain (amino acids 400–501) of murine N-Wasp (also known as Wasl) was cloned into a modified pCooFy vector with 10× histidine tag. The protein was then purified by a combination of affinity and anion exchange chromatography. In brief, the protein was expressed in a 1 liter culture of Rosetta T1 strain of BL21 cells by inducing with 0.5 mM isopropyl β-D-1-thiogalactopyranoside (IPTG) and growing the cells for 16 h at 16°C. For purification, cells were lysed by sonication. The cell lysate was purified with the His tag on a HisTrap HP column (GE Healthcare, Chicago, IL, USA) via a chromatography system. The protein-containing fractions were combined and diluted ten times for ion exchange chromatography on a MonoQ column (GE Healthcare). The selected protein fractions were buffer exchanged into phosphate buffered saline supplemented with 10% glycerol. All buffers included 1 mM tris(2-carboxyethyl)phosphine (TCEP) to prevent protein dimerization.

VCA was labeled with Atto488-maleimide (28562) from Sigma-Aldrich, St Louis, MI, USA. The dye was used in 20-fold excess of the protein (by mass) and the mix was incubated overnight in a cold room with gentle rotation. Buffer exchange was carried out on a small volume Sephadex G-25 column. This was followed by dialysis for complete removal of the dye. The final storage buffer of the protein was 50 mM Tris-HCl pH 7.5, 150 mM NaCl, 10% glycerol and 1 mM TCEP. Labeling efficiency was quantified by spectrophotometric analysis.

Purification of myosin-II from rabbit muscle, as well as labeling with Alexa Fluor 488, was carried out as described previously (Vogel et al., 2013).

Unlabeled actin monomers from rabbit skeletal muscle (AKL99) and Arp2/3 complex from porcine brain (RP01P) were purchased from Cytoskeleton, Denver, CO, USA. Actin monomers conjugated with Alexa Fluor 568 (A-12374), Alexa Fluor 488 (A-12373) and Alexa Fluor 640 (A-34051) were acquired from Thermo Fisher Scientific, Waltham, MA, USA. Capping protein CapZ (non-muscle, human recombinant) was purchased from Hypermol EK, Germany.

Blebbistatin (B0560), phosphocreatinine (P7936), creatine phosphokinase (C3755), pyranose oxidase (P4234) and catalase (C40) were purchased from Sigma-Aldrich.

Preparation of lipid bilayer

1,2-Dioleoyl-*sn*-glycero-3-phosphocholine (DOPC) and 1,2-dioleoyl-*sn*-glycero-3-[(N-(5-amino-1-carboxypentyl)iminodiacetic acid)succinyl] (nickel salt) (DGS-NTA) lipids were purchased from Avanti Polar Lipids, Alabaster, AL, USA. Atto655-labeled DOPE (1,2-dioleoyl-*sn*-glycero-3-phosphoethanolamine) was procured from ATTO-TEC GmbH, Siegen, Germany. Small unilamellar vesicles containing the desired proportion of DOPC to DGS-NTA lipids (with 0.005% Atto655-DOPE) were prepared by rehydrating a lipid film in SLB buffer (50 mM Tris-HCl pH 7.5, 150 mM KCl) followed by sonication. The composition was 99 mol% DOPC and 1 mol% DGS-NTA in all experiments, unless stated otherwise. High precision coverglass (no. 1.5, Marienfeld-Superior, Lauda-Königshofen, Germany) was treated with Piranha solution (3:1 H₂SO₄:H₂O₂, overnight), rinsed with copious amounts of milliQ water, dried and subsequently briefly treated with O₂ plasma (Femto plasma cleaner, Diener-plasma, Ebhausen, Germany). Reaction chambers were generated on these coverglasses by press-to-seal silicone isolators (Grace Bio-labs, Bend, OR, USA; procured from Sigma-Aldrich, catalogue no. GBL664206). The resulting chambers were circular (diameter 4.5 mm) with a shallow depth of 2 mm that does not

allow them to be sealed with volumes greater than 25 μ l. Then, 0.1 mg/ml of vesicles were added into the silicone chambers and mixed with rigorous pipetting to facilitate vesicle rupture and bilayer deposition. This was followed by 15 min of incubation. The bilayers were gently washed first with SLB buffer and then with VCA buffer (10 mM Tris-HCl pH 7.5, 50 mM NaCl, 1 mM DTT) and stored in this buffer until sample preparation.

For spinning disk experiments, chambers were prepared by cutting a 0.2 ml Eppendorf tube at about one-third of its height from the bottom. The lid of the tube was cut off and the mouth of the cut tube was glued to a coverslip (cleaned with the Piranha protocol) using a UV-cured adhesive (Norland Optical Adhesive 68, Norland Products, New Brunswick, NJ, USA). When the glue set, the resulting chamber was treated with plasma and the remaining protocol for bilayer deposition was followed as described above, with all volumes doubled. The advantage of these chambers is that they can be reversibly sealed by using the lid of a 1.5 ml Eppendorf microfuge tube lined with plasticine. This prevents evaporation, which was increased because of the higher incidence of the spinning disk lasers, as compared with TIRF.

Sample preparation

A lipid bilayer was flushed again with VCA buffer and then incubated with 200 nM His10-VCA in the same buffer. A premix containing actin monomers (labeled with 10% Alexa Fluor 568), Arp2/3 complex and ATP regeneration system (phosphocreatine and creatine phosphokinase) was made at the same time in G-buffer (10 mM Tris-HCl pH 8.0, 0.2 mM CaCl_2 , 0.2 mM ATP, 1 mM DTT). After 20 min, the excess VCA was washed off and actin pre-mix was added. An image was taken to obtain the reference intensity value for normalization before triggering polymerization by adding 5 \times G-to-F buffer (50 mM Tris-HCl pH 7.5, 250 mM KCl, 10 mM MgCl_2 , 1 mM DTT with variable ATP). A typical sample finally contained 1 μ M actin monomers and 10 nM Arp2/3, unless otherwise mentioned in the figures. Additionally, the sample also included the ATP regeneration system (10 mM phosphocreatinine, 53 U/ml creatine phosphokinase) and an oxygen scavenger system (3.7 U/ml pyranose oxidase, 90 U/ml catalase, 0.8% glucose). The final buffer conditions were 10 mM Tris-HCl pH 7.5, 50 mM KCl, 1 mM MgCl_2 , 1 mM DTT with ATP adjusted to 100 μ M. The sample volumes were 40 μ l.

Myofilaments were pre-assembled by making a 4 \times stock solution of the myosin in a buffer of 10 mM Tris pH 7.5, 50 mM KCl, 2 mM MgCl_2 , 1 mM DTT and incubating for 10 min before adding to the actin network by replacing one-quarter of the sample volume. If washing was required before addition of myosin, a fourfold replacement of sample volume was carried out with gentle mixing.

In all cases, evaporation was minimized by storing the samples in closed boxes containing wet tissue. For microscopy, a hydrophobic pen was used to draw a 'moat' around the silicone well and this was filled with water. A small plastic lid was used to cover the sample, including the moat, during imaging. Variations from this basic protocol are mentioned in the text, where relevant.

For experiments involving labeled VCA, Atto488-labeled VCA was mixed with unlabeled VCA to obtain a 20% labeled fraction. For labeled myosin experiments, the fraction of Alexa Fluor 488-labeled myosin-II was maintained at 1% by mixing with unlabeled myosin.

For the pulse-chase experiments shown in Fig. 5, Alexa Fluor 488-labeled actin monomers were used as the second label. Alexa Fluor 488-labeled monomers were mixed 1:10 with unlabeled actin monomers. 1 μ M of this 10% labeled actin was added to the sample, along with 10 nM Arp2/3, as described in the corresponding Results section.

In experiments requiring myosin inhibition (Fig. 6, Fig. S6A,B), blebbistatin was used at a final concentration of 20 μ M from a stock solution prepared in DMSO. Because blebbistatin is deactivated by 488 nm radiation, two-color experiments in the presence of blebbistatin were carried out with 10% Alexa Fluor 640-labeled actin monomers (Label1). The initial network was assembled with the same protocol as previously described for Alexa Fluor 568-labeled actin. After assembly, the excess monomers were washed off and myosin was introduced as previously described. For the 'before breakdown' condition, 20 μ M blebbistatin and 1 μ M of actin with 10% Alexa Fluor 568-labeled monomers (Label2) were introduced as soon as bundling was visible. In the 'after breakdown' condition, blebbistatin and Alexa Fluor 568-labeled actin were introduced after considerable intensity reduction of the Alexa Fluor 640-actin network.

When the chambers made with microfuge tubes were used for spinning disk confocal microscopy, the protocol was identical, but the reaction volume was doubled.

Image acquisition

Fluorescence images were recorded on a home-built objective-type TIRF microscope (Mücksch et al., 2018), constructed around a Nikon Ti-S microscope body with oil immersion objective (Nikon SR Apo TIRF, 100 \times , NA 1.49; Nikon, Düsseldorf, Germany). In brief, the excitation laser lines [490 nm (Cobolt Calypso, 50 mW nominal), 561 nm (Cobolt Jive, 50 mW nominal) and 640 nm (Cobolt 06-MLD, 140 mW nominal)] were attenuated with an acousto-optical tunable filter (AOTF; Gooch & Housego TF-525-250) and spatially filtered by a polarization-maintaining single-mode fiber (kineFLEX-P-3-S-405.640-0.7-FCS-P0 and kineMATIX; Qioptiq, Hamble, UK). After the fiber, the excitation beam was collimated, extended threefold by a telescope of achromatic doublets and moved off the optical axis by a mirror and a focusing lens, both on a piezo-controlled translation stage. This way, the excitation beam was focused off-axis on the back focal plane of the objective. Excitation and emission light were separated using a four-color notch beam splitter (zt405/488/561/640rpc flat; AHF Analysentechnik, Tübingen, Germany). For single-color detection, the fluorescent light passed through a 4f lens system, including spectral filtering (525/50, 593/46, 705/100), and was detected on an electron-multiplying charge-coupled device (EMCCD) camera (iXon Ultra 897; Andor Technologies, Belfast, UK). For dual-color schemes, the image was laterally clipped in a conjugated focal plane. The clipped images were spectrally separated (T555LPXR, Chroma), bandpass filtered (525/50, 593/46) and focused side-by-side on the same EMCCD. To minimize phototoxicity and photobleaching, the AOTF transmission was synchronized with the EMCCD acquisition using a controller card (PCIe-6323, National Instruments) with customized LabView software (National Instruments, Austin, USA). The imaging interval was usually 5 s, with exposure times of 50 ms. In some cases, imaging was carried out at 2 or 10 s intervals or the exposure time was increased to 100 ms. For high temporal resolution in Movie 8, imaging was done at 200 ms intervals with a 50 ms exposure time. Drift of the focus position was eliminated using a custom-built focus stabilization system, based on a feedback loop that monitored the position of an infrared laser beam, back-reflected from the sample interface.

For imaging in the z-axis (Fig S3A,B, Fig S4E), a Yokogawa scan head CSU10-X1 spinning disk system set up on a Nikon Eclipse Ti inverted microscope body was used. Detection was carried out with an EMCCD camera (iXon Ultra 897; Andor Technologies, Belfast, UK). A 3i solid state diode laser stack with 488, 561 and 640 nm laser lines (Intelligent Imaging Innovations, Denver, Colorado, USA) was used for excitation. Imaging was carried out using a UPLanSApo 60 \times /1.20 Water UIS2 objective (Olympus, Japan).

Video data for fluorescence recovery after photobleaching (FRAP) analysis of VCA was acquired on a VectorTIRF system equipped with a FRAP unit (3i; Intelligent Imaging Innovations) using a Nikon 60 \times , N.A. 1.49 objective and 488/640 nm excitation.

Image processing and analysis

ImageJ (Rueden et al., 2017; <https://imagej.nih.gov/ij/>) was used for image processing and analysis.

Rolling ball background subtraction was used to highlight features in Fig. 2A and Fig. S3Ec. Rolling ball radii were 100 pixels for actin and 20 pixels for myosin. For Movie 8, a walking average over three frames was generated to highlight actin structures. The WalkingAverage plugin was obtained from the EMBL webpage (<https://www.embl.de/eamnet/html/kymograph.html>).

For intensity measurement, the customized macro included a module to specify a square region (edge length 200 pixels) of the sample and then measure mean intensity and standard deviation for each frame. For calculation of coefficient of variance in Fig. 3, the ratio between the mean intensity and the standard deviation was calculated for a square of edge length 350 pixels for each time frame.

For length scale analyses, contraction foci were visually identified on the basis of intensity distributions. During coarsening, these appeared as a bright actin cluster of undefined shape. During homogeneous contraction,

the foci appeared as static points surrounded by dynamic actin filaments. The latter could be identified more easily in images with temporal color coding of a few time frames (e.g., in Fig. S5B), where they appeared as white points due to the colocalization of all colors of the LUT 'Spectrum'. The multipoint selection tool was used to indicate the roughly estimated centers of the nearest neighbors of each foci. A custom-made macro then carried out the mathematical transformation of the pixel positions to lengths in microns in a pairwise manner and marked the foci that had already been measured to exclude them from subsequent iterations.

Additional plugins used were Radial_Profile_Angle_Ext and Kymo_wide_reslice (available for download from <https://imagej.nih.gov>). The radial intensity profiles in Fig. 2D were obtained using the Radial_Profile_Angle_Ext plugin, which integrates the intensities at each point along the radius of a circular selection. The profiles were mirrored to plot the average intensity along the diameter for aiding visualization of the node organization. For Kymo_wide_reslice, the pixel thickness of the selected line was specified with corresponding data in the figure legend.

For FRAP analysis, intensity traces of bleached and control regions were extracted using 3i's proprietary SlideBook 6.0 software. Intensity traces of bleached regions were normalized to the control region intensities by division to correct for (small) overall sample drift and bleaching, normalized to the first data point, and fitted with a single exponential to extract the mobile fraction and recovery half times.

For analysis of the dynamic steady state (Fig. 4), all analysis and plotting was done in MATLAB (R2016b, Mathworks) using custom-written scripts. For Fig. 4A, the image correlation between frame_t and frame₁ was calculated for the entire videos using the in-built function corr2. The same function was used for Fig. 4B, correlating frame_t and frame_{t+x}, with *x* being the time window noted in the figure. For generating the quiver plots (Fig. 4C, second and third row), images were binned by a factor of 8, and the gradient in *x,y* (dx,dy) calculated for each frame. The arrows in the quiver plot correspond to the vectorial difference of the (dx,dy,t_x) and (dx,dy,t_{x+25s}) of subsequent frames t_x,t_{x+25s} at time point *x* indicated in the figure. For Fig. 4C, last row, the pixel-wise intensity gradient in time (*dt*) was calculated for all pixels of frames t_x,t_{x+25s} from the same binned videos, normalized to the maximum value in the entire frame and plotted as a heat map.

The software FFmpeg was used for making movies from time series data (available for download from <http://ffmpeg.org/>).

Statistical analysis and plotting of graphs was done using Origin. Fitting of curves for actin growth profiles was also done in Origin using the in-built model ExpGrow1. Fitting excluded the initial 3 min to achieve a better fit. For significance testing in length scale measurements, values were pooled across samples for each condition. The nonparametric Mann–Whitney U test was used to compare two populations at a 0.05 significance level.

Acknowledgements

The authors would like to thank Prof. Klemens Rotner for sharing plasmids, and Sigrid Bauer, Dr Katharina Nakel, Michaela Schaper and Kerstin Andersson for technical assistance. S., J.M. and P.B. acknowledge support from the International Max Planck Research School for Molecular and Cellular Life Sciences (IMPRS-LS). J.M. and P.B. acknowledge support from the Center for NanoScience (CeNS).

Competing interests

The authors declare no competing or financial interests.

Author contributions

Conceptualization: S., K.A.G., S.K.V.; Methodology: S., K.A.G., J.M., P.B.; Software: S., K.A.G., J.M., P.B.; Validation: S., K.A.G.; Formal analysis: S., K.A.G.; Investigation: S., K.A.G.; Resources: S.K.V., J.M., P.B.; Writing - original draft: S.; Writing - review & editing: S., K.A.G., S.K.V., J.M., P.B., P.S.; Visualization: S., K.A.G.; Supervision: P.S.; Project administration: S., K.A.G., S.K.V.; Funding acquisition: K.A.G., S.K.V., P.S.

Funding

S. and S.K.V. received funding from the MaxSynBio Consortium, which is jointly funded by the Federal Ministry of Education and Research of Germany (Bundesministerium für Bildung und Forschung, BMBF) and the Max Planck Society (Max-Planck-Gesellschaft, MPG). K.A.G. received funding from the European Union's Horizon 2020 research and innovation program under the Marie Skłodowska-Curie grant agreement [no. 703132]. S.K.V. is grateful for the financial

support by the Daimler und Benz Stiftung (Project Grant PSBioc8216). J.M. is grateful for financial support from the excellence cluster Nanosystems Initiative Munich, which is funded by the Deutsche Forschungsgemeinschaft (DFG).

Supplementary information

Supplementary information available online at <http://jcs.biologists.org/lookup/doi/10.1242/jcs.219899.supplemental>

References

- Akin, O. and Mullins, R. D. (2008). Capping protein increases the rate of actin-based motility by promoting filament nucleation by the Arp2/3 complex. *Cell* **133**, 841–851.
- Andrianantoandro, E., Blanchoin, L., Sept, D., Mccammon, J. A. and Pollard, T. D. (2001). Kinetic mechanism of end-to-end annealing of actin filaments. *J. Mol. Biol.* **312**, 721–730.
- Backouche, F., Haviv, L., Groswasser, D. and Bernheim-Groswasser, A. (2006). Active gels: dynamics of patterning and self-organization. *Phys. Biol.* **3**, 264–273.
- Bieling, P., Hansen, S. D., Akin, O., Li, T. D., Hayden, C. C., Fletcher, D. A. and Mullins, R. D. (2018). WH2 and proline-rich domains of WASP-family proteins collaborate to accelerate actin filament elongation. *EMBO J.* **37**, 102–121.
- Blanchoin, L., Pollard, T. D. and Mullins, R. D. (2000). Interactions of ADF/cofilin, Arp2/3 complex, capping protein and profilin in remodeling of branched actin filament networks. *Curr. Biol.* **10**, 1273–1282.
- Bussonnier, M., Carvalho, K., Lemièrre, J., Joanny, J.-F., Sykes, C. and Betz, T. (2014). Mechanical detection of a long-range actin network emanating from a biomimetic cortex. *Biophys. J.* **107**, 854–862.
- Carvalho, K., Tsai, F.-C., Lees, E., Voituriez, R., Koenderink, G. H. and Sykes, C. (2013). Cell-sized liposomes reveal how actomyosin cortical tension drives shape change. *Proc. Natl. Acad. Sci. USA* **110**, 16456–16461.
- Fritzsche, M., Lewalle, A., Duke, T., Kruse, K. and Charras, G. (2013). Analysis of turnover dynamics of the submembranous actin cortex. *Mol. Biol. Cell* **24**, 757–767.
- Fritzsche, M., Thorogate, R. and Charras, G. (2014). Quantitative analysis of ezrin turnover dynamics in the actin cortex. *Biophys. J.* **106**, 343–353.
- Guha, M., Zhou, M. and Wang, Y.-L. (2005). Cortical actin turnover during cytokinesis requires myosin II. *Curr. Biol.* **15**, 732–736.
- Haviv, L., Gillo, D., Backouche, F. and Bernheim-Groswasser, A. (2008). A cytoskeletal demolition worker: myosin II acts as an actin depolymerization agent. *J. Mol. Biol.* **375**, 325–330.
- Higgs, H. N. and Pollard, T. D. (2000). Activation by Cdc42 and PIP(2) of Wiskott-Aldrich syndrome protein (WASP) stimulates actin nucleation by Arp2/3 complex. *J. Cell Biol.* **150**, 1311–1320.
- Köhler, S., Schaller, V. and Bausch, A. R. (2011). Structure formation in active networks. *Nat. Mater.* **10**, 462–468.
- Köster, D. V., Husain, K., Iljazi, E., Bhat, A., Bieling, P., Mullins, R. D., Rao, M. and Mayor, S. (2016). Actomyosin dynamics drive local membrane component organization in an in vitro active composite layer. *Proc. Natl. Acad. Sci. USA* **113**, E1645–E1654.
- Linsmeier, I., Banerjee, S., Oakes, P. W., Jung, W., Kim, T. and Murrell, M. P. (2016). Disordered actomyosin networks are sufficient to produce cooperative and telescopic contractility. *Nat. Commun.* **7**, 12615.
- Machesky, L. M., Mullins, R. D., Higgs, H. N., Kaiser, D. A., Blanchoin, L., May, R. C., Hall, M. E. and Pollard, T. D. (1999). Scar, a WASP-related protein, activates nucleation of actin filaments by the Arp2/3 complex. *Proc. Natl. Acad. Sci. USA* **96**, 3739–3744.
- Martin, A. C., Kaschube, M. and Wieschaus, E. F. (2009). Pulsed contractions of an actin-myosin network drive apical constriction. *Nature* **457**, 495–499.
- Medeiros, N. A., Burnette, D. T. and Forscher, P. (2006). Myosin II functions in actin-bundle turnover in neuronal growth cones. *Nat. Cell Biol.* **8**, 216–226.
- Mücksch, J., Blumhardt, P., Strauss, M. T., Petrov, E. P., Jungmann, R. and Schwille, P. (2018). Quantifying reversible surface binding via surface-integrated fluorescence correlation spectroscopy. *Nano Lett.* **18**, 3185–3192.
- Murphy, D. B., Gray, R. O., Grasser, W. A. and Pollard, T. D. (1988). Direct demonstration of actin filament annealing in vitro. *J. Cell Biol.* **106**, 1947–1954.
- Murrell, M. P. and Gardel, M. L. (2012). F-actin buckling coordinates contractility and severing in a biomimetic actomyosin cortex. *Proc. Natl. Acad. Sci. USA* **109**, 20820–20825.
- Murthy, K. and Wadsworth, P. (2005). Myosin-II-dependent localization and dynamics of F-actin during cytokinesis. *Curr. Biol.* **15**, 724–731.
- Nishikawa, M., Naganathan, S. R., Jülicher, F. and Grill, S. W. (2017). Controlling contractile instabilities in the actomyosin cortex. *eLife* **6**, e19595.
- Nye, J. A. and Groves, J. T. (2008). Kinetic control of histidine-tagged protein surface density on supported lipid bilayers. *Langmuir* **24**, 4145–4149.
- Pantaloni, D., Boujemaâ, R., Didry, D., Gounon, P. and Carlier, M.-F. (2000). The Arp2/3 complex branches filament barbed ends: functional antagonism with capping proteins. *Nat. Cell Biol.* **2**, 385–391.
- Reymann, A.-C., Martiel, J.-L., Cambier, T., Blanchoin, L., Boujemaâ-Paterski, R. and Théry, M. (2010). Nucleation geometry governs ordered actin networks structures. *Nat. Mater.* **9**, 827–832.

- Reymann, A.-C., Boujemaa-Paterski, R., Martiel, J.-L., Guerin, C., Cao, W., Chin, H. F., De La Cruz, E. M., Thery, M. and Blanchoin, L. (2012). Actin network architecture can determine myosin motor activity. *Science* **336**, 1310-1314.
- Rohatgi, R., Ma, L., Miki, H., Lopez, M., Kirchhausen, T., Takenawa, T. and Kirschner, M. W. (1999). The interaction between N-WASP and the Arp2/3 complex links Cdc42-dependent signals to actin assembly. *Cell* **97**, 221-231.
- Rueden, C. T., Schindelin, J., Hiner, M. C., DeZonia, B. E., Walter, A. E., Arena, E. T. and Eliceiri, K. W. (2017). ImageJ2: ImageJ for the next generation of scientific image data. *BMC Bioinformatics* **18**, 529.
- Salbreux, G., Charras, G. and Paluch, E. (2012). Actin cortex mechanics and cellular morphogenesis. *Trends Cell Biol.* **22**, 536-545.
- Smith, D., Ziebert, F., Humphrey, D., Duggan, C., Steinbeck, M., Zimmermann, W. and Käs, J. (2007). Molecular motor-induced instabilities and cross linkers determine biopolymer organization. *Biophys. J.* **93**, 4445-4452.
- Soares e Silva, M., Depken, M., Stuhrmann, B., Korsten, M., Mackintosh, F. C. and Koenderink, G. H. (2011). Active multistage coarsening of actin networks driven by myosin motors. *Proc. Natl. Acad. Sci. USA* **108**, 9408-9413.
- Stam, S., Freedman, S. L., Banerjee, S., Weirich, K. L., Dinner, A. R. and Gardel, M. L. (2017). Filament rigidity and connectivity tune the deformation modes of active biopolymer networks. *Proc. Natl. Acad. Sci. USA* **114**, E10037-E10045.
- Tinevez, J.-Y., Schulze, U., Salbreux, G., Roensch, J., Joanny, J.-F. and Paluch, E. (2009). Role of cortical tension in bleb growth. *Proc. Natl. Acad. Sci. USA* **106**, 18581-18586.
- Vogel, S. K., Petrasek, Z., Heinemann, F. and Schwille, P. (2013). Myosin motors fragment and compact membrane-bound actin filaments. *eLife* **2**, e00116.
- Vogel, S. K., Greiss, F., Khmelinskaia, A. and Schwille, P. (2017). Control of lipid domain organization by a biomimetic contractile actomyosin cortex. *eLife* **6**, e24350.
- Wilson, C. A., Tsuchida, M. A., Allen, G. M., Barnhart, E. L., Applegate, K. T., Yam, P. T., Ji, L., Keren, K., Danuser, G. and Theriot, J. A. (2010). Myosin II contributes to cell-scale actin network treadmilling through network disassembly. *Nature* **465**, 373-377.
- Yang, Q., Zhang, X.-F., Pollard, T. D. and Forscher, P. (2012). Arp2/3 complex-dependent actin networks constrain myosin II function in driving retrograde actin flow. *J. Cell Biol.* **197**, 939-956.